Afterglow Molecular Imaging Using Bright, Biodegradable Polymer Nanoparticles

Qingqing Miao,[1] Chen Xie,[1] Xu Zhen,[1] Yan Lyu,[1] Hongwei Duan,[1] Xiaogang Liu,[2] Jesse V. Jokerst,[3] and Kanyi Pu[1,*]

[1]School of Chemical and Biomedical Engineering, Nanyang Technological University, Singapore, 637457.

[2]Department of Chemistry, National University of Singapore, Singapore 117543.

[3]Department of NanoEngineering, University of California San Diego, La Jolla, California 92093-0448, USA.

*E-mail: kypu@ntu.edu.sg

Abstract. Optical agents that can emit long-lasting light after cessation of excitation have great promise for ultrasensitive *in vivo* imaging due to eliminated tissue autofluorescence. However, such imaging agents are rare and generally limited to inorganic nanoparticles with relatively low brightness and short near-infrared (NIR) emission. Here, we introduce a new generation of purely organic agents based on semiconducting polymer nanoparticles (SPNs) that can store photon energy via chemical defects and then emit long NIR afterglow luminescence at 780 nm after light irradiation. The *in vivo* afterglow of SPNs is more than two orders of magnitude brighter than that of concentration-matched inorganic agents, and the signal is detectable through an entire live mouse—a feat that is nearly impossible with NIR fluorescence imaging. The bright NIR afterglow of SPNs allows for high-contrast lymph node imaging in living mice, with a signal-to-background ratio that is 127-times higher than that obtained by NIR fluorescence imaging. The significantly enhanced contrast also permits much faster delineation of tumor in murine models after systematic administration relative to NIR fluorescence imaging. Moreover, the structural versatility of SPNs enables, for the first time, an activatable afterglow probe with signal specific to the presence of biothiols permitting excitation-free real-time imaging of drug-induced hepatotoxicity in living mice. This study provides the basis for an entirely new class of optical reporters for molecular imaging at a sensitivity level not achievable with conventional NIR fluorescence imaging.

Introduction

Optical imaging plays a crucial role in biology and medicine[1]; however, the need for real-time light excitation during imaging produces tissue autofluorescence, which compromises imaging sensitivity and specificity in living subjects[2]. Thereby, optical imaging strategies such as bioluminescence and Cerenkov luminescence that eliminate the need for concurrent light excitation have attracted tremendous interests in molecular imaging[3, 4]. However, bioluminescence probes require enzyme/substrate to produce light emission, and thus their signals are often affected by enzyme microenvironment and substrate biodistribution in living animals[5]. In contrast, Cerenkov probes rely on the release of charged particles from radioisotopes, which involve complicated synthetic procedure and exhibit short lifetime[6].

Afterglow luminescence is an intrinsic luminescent process that occurs after the end of light excitation[7]. Afterglow luminescence is generally caused by the slow releases of photons from energy traps in the materials upon thermal simulation. Although afterglow imaging has tremendous promise for *in vivo* imaging because of the lack of real-time excitation, only a few inorganic nanoparticles have been shown to produce afterglow in biologically relevant conditions[8-10]—all of these contain rare-earth heavy metal ions such as europium, praseodymium and chromium (**Supplementary Table 1**)[11-16]. Thus, the current generation of afterglow probes are significantly hampered due to toxicity concerns[17].

Inorganic afterglow nanoparticles are currently utilized as accumulation probes and have limited targeting applications[7-9] due to the difficulty in surface modifications. Thus, contrast is determined by the difference in probe concentration between target tissue and adjacent normal tissue. In contrast to concentration differences, smart activatable probes that undergo a signal intensity change upon detecting molecular targets offer high contrast and real-time information on pathological conditions at the molecular level[18, 19]. Thus, it is somewhat surprising that the benefits of afterglow imaging and activatable probes have not yet been combined for *in vivo* imaging.

In this study, we report the design and application of semiconducting polymer nanoparticles (SPNs) as afterglow luminescence probes for molecular imaging in living mice. SPNs are built from optically-active semiconducting polymers (SPs) and are an alternative class of photonic nanomaterials[20]. They are completely organic and contain biologically benign ingredients to overcome metal-ion-induced toxicity[21]. Due to their structural flexibility and excellent optical properties, SPNs can be utilized as fluorescence, chemiluminescence, bioluminescence or photoacoustic agents for a variety of *in vivo* applications including tumor imaging[22], neuroinflammation imaging[23], lymph node mapping[24], ultrafast hemodynamic imaging[25] and neuron activation[26, 27]. While we recently observed the afterglow phenomenon in a SPN, its mechanism and *in vivo* utility remain unexplored[28].

Here, we first investigate the mechanism of SPN afterglow luminescence and find that it involves light-induced formation of unstable chemical defects that can produce photons as downstream products. We then propose a strategy to effectively amplify and red-shift the afterglow of the SPNs and use it for lymph node imaging in living mice. Finally, we demonstrate the feasibility to develop SPNs into activatable afterglow molecular probes for *in vivo* monitoring of drug-induced hepatotoxicity. Thus, this study not only reveals fundamental guidelines for developing organic afterglow nanoparticles, but also provides the first generation of activatable molecular probes with afterglow signal readouts for advanced molecular imaging.

Results

Screening of SPs for Afterglow

SPs with different molecular structures were tested to identify structures in favor of afterglow luminescence (**Fig. 1**a). Nanoprecipitation was used to transform seven SPs into water-soluble nanoparticles in the presence of an amphiphilic triblock copolymer (PEG-*b*-PPG-*b*-PEG) (**Fig. 1**b). The hydrodynamic diameters of the SPNs measured by dynamic light scattering (DLS) were similar ranging from 30 to 40 nm (**Fig. 1**c). Transmission electron microscopy (TEM) further confirmed the spherical morphology with an average diameter of 33.9 ± 4.3 nm (**Fig. 1**d), which was nearly identical to the DLS data. The nanoparticle solutions were translucent (**Fig. 1**e) with no precipitates or size changes even after two months of storage (**Supplementary Fig. 1**) suggesting excellent stability in aqueous solution.

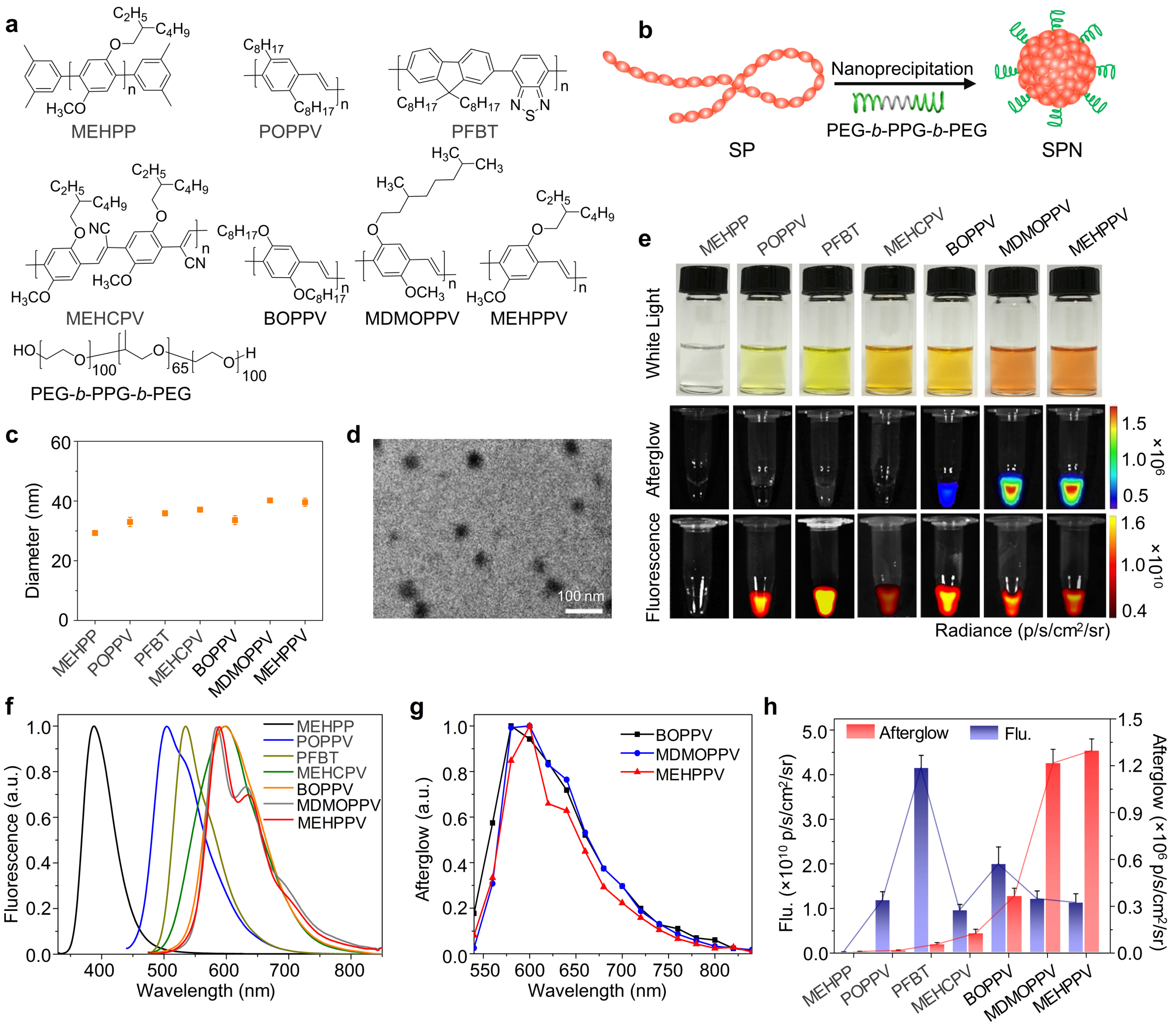

Figure 1. Synthesis and characterization of SPNs. (a) Chemical structures of the SPs (MEHPP, POPPV, PFBT, MEHCPV, BOPPV, MDMOPPV and MEHPPV) and the amphiphilic triblock copolymer (PEG-*b*-PPG-*b*-PEG) used for the synthesis of SPNs. **(b)** Schematic illustration of the preparation of SPNs through nanoprecipitation. **(c)** Average hydrodynamic diameters of SPNs in 1×PBS buffer (pH = 7.4). **(d)** Representative TEM image of SPN-MEHPPV. **(e)** White-light (up panel), afterglow luminescence (middle panel) and fluorescence (bottom panel) images of SPN-MEHPP, SPN-POPPV, SPN-PFBT, SPN-MEHCPV, SPN-BOPPV, SPN-MDMOPPV and SPN-MEHPPV in 1×PBS buffer (pH = 7.4). The fluorescence and afterglow images of SPNs were taken at the same absorption intensities at their respective maximum (the absorption is 0.5 after 10-fold dilution of the solution). The fluorescence images were acquired upon excitation at 465 nm for all SPNs except for SPN-MEHPP and SPN-POPPV (430 nm). The afterglow images were acquired for 30 s after the pre-irradiation of SPNs under white light at a power density of 0.1 W/cm^2 for 1 min. **(f)**

Normalized fluorescence spectra of SPNs in 1×PBS buffer (pH = 7.4). **(g)** Normalized afterglow luminescence spectra of SPN-BOPPV, SPN-MDMOPPV and SPN-MEHPPV in 1×PBS buffer (pH = 7.4). **(h)** Quantification of fluorescence and afterglow intensities of SPNs in Fig. 1e.

The fluorescence and afterglow signals of SPNs were collected with an IVIS Spectrum imaging system under fluorescence (with excitation) and bioluminescence (without excitation) modes, respectively. Only PPV-based SPNs including BOPPV, MDMOPPV and MEHPPV showed obvious afterglow luminescence (**Fig. 1**e,h); their luminescence spectral profiles were similar to the fluorescence spectra (**Fig. 1**f,g). However, all SPNs were highly fluorescent (**Fig. 1**e,f). The fluorescence of SPN-MEHPP was undetectable because its absorption wavelength is too short to be excited by IVIS Spectrum imaging system (**Supplementary Fig. 2**).

Afterglow signal was only seen in PPV-based SPs suggesting that phenylenevinylene plays an essential role in the production of this real-time, excitation-free luminescence. However, some PPV-based SPs including SPN-MEHCPV and SPN-POPPV did not emit detectable afterglow luminescence suggesting that the substituents on the PPV backbone are also important. Similar afterglow behaviors were observed for SPs dispersed in THF (**Supplementary Fig. 3**). This confirms that the chemical structure of SP rather than the nanoparticle structure controls SPN afterglow.

Mechanistic Study of Afterglow

To identify the underlying mechanism governing SPN afterglow luminescence, we studied the effect of light irradiation on the chemical structures of SPs. The absorption peak of MEHPPV at 493 nm showed a remarkable hypochromatic shift and an intensity decrease after irradiation indicating a breakdown in the conjugation length and thus the decomposition of

MEHPPV (**Fig. 2**a). Proton nuclear magnetic resonance (^1H NMR) analysis showed two new peaks at 9.88 and 10.47 ppm after light irradiation (**Fig. 2**b). These were assigned to the aldehyde and carboxyl peaks, respectively. Peak broadening and division are caused by different chemical environments and indicate the formation of inhomogeneous fragments. The characteristic peaks of oxidized MEHPPV fragments were also detected in Fourier transform infrared spectroscopy (FTIR) at 1728 cm^{-1}. In addition, the peak at 3053 cm^{-1} corresponding to ethene-1,2-diyl groups attenuated after light irradiation, further proving the oxidation of vinylene bonds. Similar spectral changes were also observed for BOPPV and MDMOPPV (**Supplementary Fig. 4**) but other SPs didn't show obvious change (**Supplementary Fig. 5**). Thus, these data clearly suggest that light irradiation oxidizes vinylene bonds in some PPVs to break them into inhomogeneously oxidized fragments.

Next, a singlet oxygen sensor green (SOSG) was applied to test for the generation of singlet oxygen ($^1O_2$) during light-induced oxidation. After light irradiation of the SPN-MEHPPV solution for 5 min, the fluorescence intensities of SOSG at 528 nm increased 1.69-fold (**Fig. 2**d). This proved that $^1O_2$ was produced during irradiation and was responsible for the oxidization of MEHPPV. Thereby, the mechanism of afterglow luminescence of PPV-based SPNs is proposed as shown in **Fig. 2**g. Light irradiation of PPVs generates $^1O_2$ that oxidize the vinylene bond (C=C) via π^2-π^2 cycloaddition to form a PPV-dioxetane intermediate. This intermediate is unstable[29] and can spontaneously degrade into an PPV-aldehyde and generate photons. Further oxidation of the PPV-aldehyde yields PPV-carboxyl as the final product of the light-irradiation reaction. Thus, the key step in afterglow luminescence is $^1O_2$-induced formation of PPV-dioxetane, which is determined by the oxidative sensitivity of the vinyl bond in PPVs. This explains why not all PPV-based SPNs had afterglow as well as the role of the substituent. In fact, only PPVs with electron-donating substituents (alkoxyl groups) including BOPPV, MDMOPPV and MEHPPV showed detectable afterglow luminescence. Other derivatives with weak electron-donating (alkyl groups for POPPV) or strong electron-withdrawing substituents (cyano groups for MEHCPV) did not.

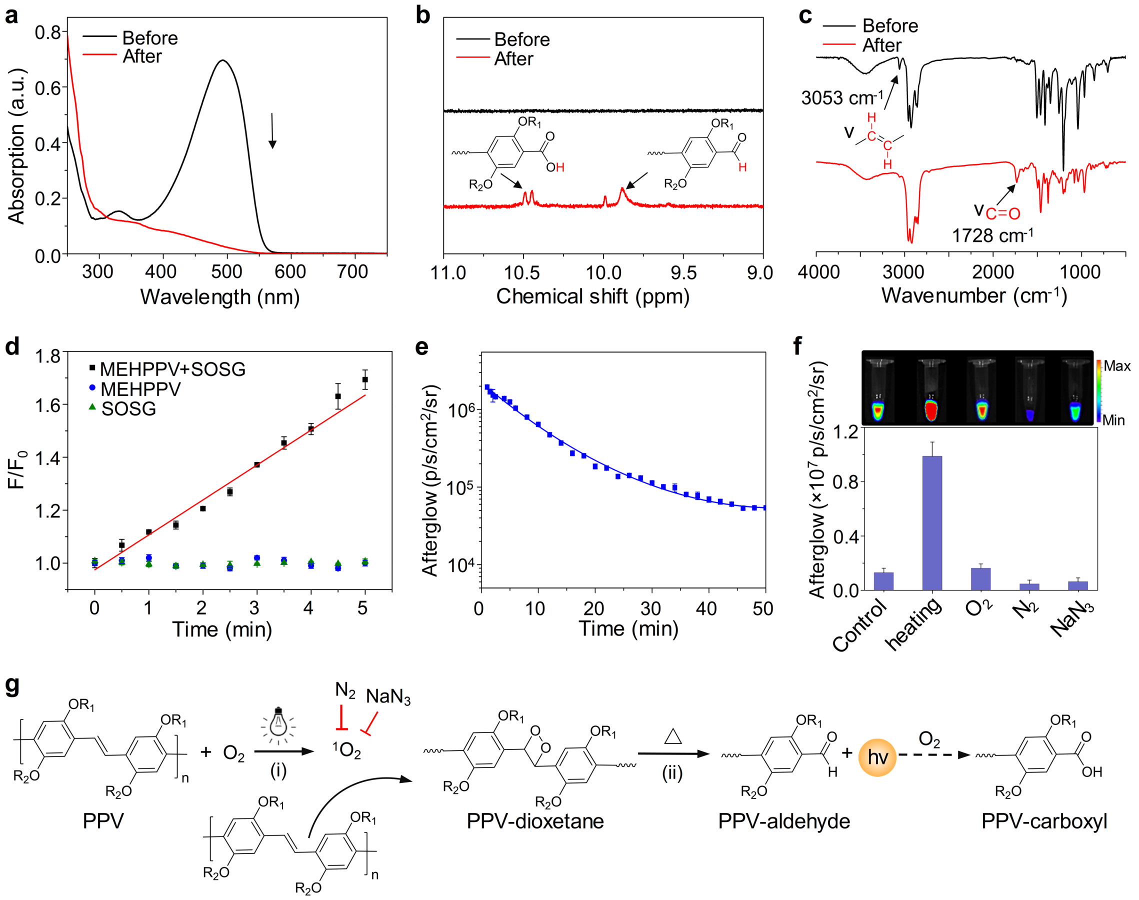

Figure 2. Mechanistic study of the afterglow of SPNs. (a) UV-Vis absorption spectra of MEHPPV (10 μg/mL) before and after light irradiation for 4 h in $CHCl_3$ (power: 0.1 W/cm^2). **(b)** ^{1}H NMR spectra of MEHPPV before and after light illumination for 24 h in $CDCl_3$ (power: 0.1 W/cm^2). **(c)** FTIR spectra of MEHPPV before and after light illumination 24 h in $CHCl_3$ (power: 0.1 W/cm^2). **(d)** Fluorescence enhancement (F/F$_0$) of SOSG (1 μM) at 528 nm in the absence or presence of SPN-MEHPPV (1.25 μg/mL) as a function of light irradiation time. **(e)** Decay of afterglow luminescence of SPN-MEHPPV (62.5 μg/mL) at room temperature. The nanoparticle solution was pre-illuminated for 1 min under white light at a power density of 0.1 W/cm^2 before

the collection of afterglow signals. **(f)** Afterglow images and intensities of SPN-MEHPPV (62.5 μg/mL) acquired at different temperatures (room temperature and 60 ºC), after treatment by N_2, O_2 purging or in the presence of 50 $_{w/w}$% NaN_3. **(g)** Proposed mechanism for the afterglow luminescence of PPV-based SP

The afterglow luminescence of PPV-based SPNs is long lasting with a half-life of 6.6 min at biologically relevant conditions (pH = 7.4 at 37 ºC) (**Fig. 2**e). The afterglow conditions can be controlled by changing the reaction conditions including temperature and oxygen levels as well as the addition of an $^1O_2$ scavenger. By intervention in the first pre-light-irradiation step (**Fig. 2**f), the afterglow of SPN-MEHPPV could be increased 1.25-fold or decreased by 2.82-fold when measured in O_2- and N_2-saturated solutions, respectively. Moreover, the addition of the $^1O_2$ scavenger (NaN_3) could reduce the afterglow intensity by 2.06-fold. By intervention in the second decomposition step (**Fig. 2**f), the afterglow intensity could be promoted by 5-fold upon elevating the temperature from 37 to 60 ºC. It was nearly completely inhibited at 0 ºC (**Supplementary Fig. 6**). Similar afterglow behaviours were observed for SPN-MDMOPPV and SPN-BOPPV (**Supplementary Fig. 6**). Taken together, these data not only further validated the proposed mechanism of afterglow but also highlighted the important role of the $^1O_2$ species in determining the afterglow brightness of SPNs.

Optimization of Afterglow

The NIR light ranging from 700 to 2,500 nm penetrates biological tissues more efficiently than visible light due to reduced tissue scattering and minimized biological autofluorescence in this region[2]. To amplify afterglow and red-shift it into the ideal NIR optical imaging window, a $^1O_2$ sensitizer, silicon 2,3-naphthalocyanine bis(trihexylsilyloxide) (NCBS), was doped into SPN-MEHPPV *via* nanoprecipitation (**Fig. 3**a). Because NCBS can absorb in the NIR region

(**Supplementary Fig. 7**a), it induces afterglow by pre-irradiation at 808 nm. Thus, SPNs with different weight percentages of NCBS (1, 2.5, 5 and 10 $_{w/w}$%) were prepared and defined as SPN-NCBS1, SPN-NCBS2.5, SPN-NCBS5 and SPN-NCBS10, respectively. Doping had no obvious effect on the size and morphology of the SPNs (**Supplementary Fig. 8**). The MEHPPV fluorescence at 580 nm gradually decreased with increasing doping concentration along with a gradual increase in NCBS emission at 775 nm (**Fig. 3**d,f and **Supplementary Fig. 9**). This spectral change confirmed the efficient energy transfer from MEHPPV to NCBS. Saturation occurred at 5%—further increases in doping concentration decreased the emission of NCBS (**Supplementary Fig. 9**) due to the self-quenching of NCBS at elevated local concentrations within the nanoparticles.

In contrast, regardless of the pre-irradiation laser wavelength (808 or 514 nm), the afterglow intensities at both 590 and 775 nm continuously increased with increasing doping concentration (**Fig. 3**c,e,f). The laser irradiation conditions were optimized (**Supplementary Fig. 10**). Signal quantification showed that the absolute afterglow intensities induced by pre-irradiation at 514 nm increased by 6.8-fold when comparing the optimal SPN (SPN-NCBS5) with the non-doped control SPN (SPN-MEHPPV) (**Fig. 3**f). Moreover, the afterglow of SPN-NCBS5 could be further enhanced by 11-fold at 808 nm versus 514 nm at the same power density (**Fig. 3**b,c,e,f). This was attributed to NCBS' stronger ability to generate $^1O_2$ relative to MEHPPV (**Supplementary Fig. 11**). No afterglow was detected for the nanoparticles composed of NCBS5 only (**Supplementary Fig. 9**c). The $^1O_2$ sensitizer-amplified afterglow was also observed for tetraphenyl porphyrine (TPP)-doped SPN-MEHPPV and NCBS- or TPP-doped SPN-MDMOPPV (**Supplementary Figs 12** and **13**). These data suggest that $^1O_2$ sensitizers are intraparticle promoters to effectively amplify the afterglow of SPNs and modulate their emission wavelengths.

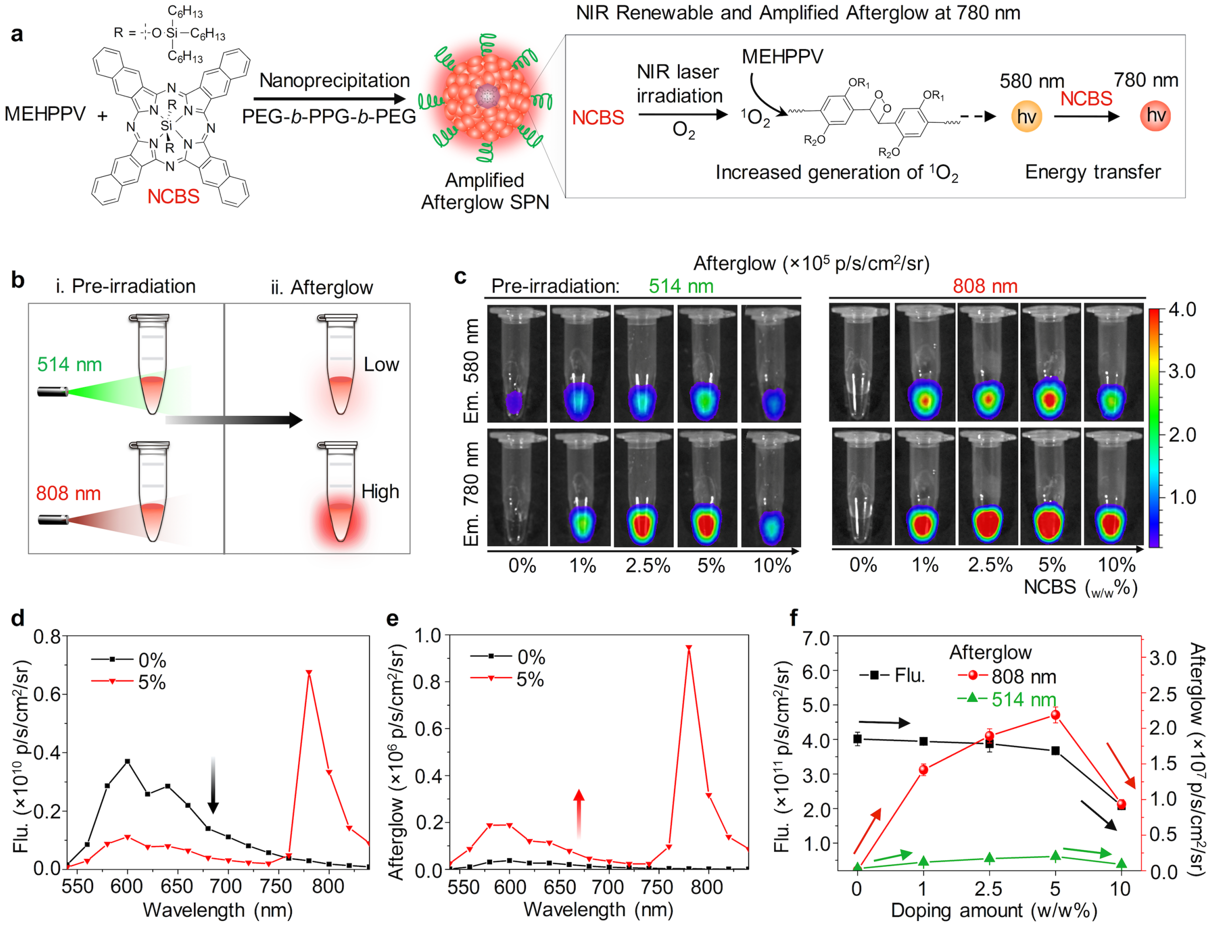

Figure 3. **$^1O_2$-sensitizer amplified NIR afterglow.** (**a**) Schematic illustration of the proposed mechanism for $^1O_2$-sensitizer-amplified NIR afterglow. (**b**) Schematic illustration of SPN-NCBS pre-irradiated by an 808 nm laser for afterglow enhancement versus a 514 nm laser. (**c**) Afterglow luminescence images of 12.5 μg/mL SPN-NCBS (based on the mass of MEHPPV) pre-irradiated at 514 (left) or 808 nm (right). The afterglow images were acquired under bioluminescence model with an acquisition time of 30 s. The nanoparticle solutions were pre-irradiated by 808 or 514 nm laser (1 W/cm^2) for 1 min, and then the images were collected for 5 s after removal of the laser source. Fluorescence (**d**) and NIR-induced afterglow luminescence spectra (**e**) of SPN-MEHPPV and SPN-NCBS5 in 1×PBS buffer (pH = 7.4). (**f**) Quantification of the absolute fluorescence and afterglow luminescence intensities of SPN-MEHPPV at different doping amounts of NCBS. The error bars represent the standard

deviation (n = 3).

Tissue Penetration Study of Afterglow

The suitability of the amplified afterglow nanoparticle (SPN-NCBS5) for biological applications was first verified by the good cytocompatibility of SPN-NCBS5 (**Supplementary Fig. 14**). The penetration depth and imaging sensitivity for the afterglow of SPN-NCBS5 were then examined both *in vitro* and *in vivo*. Because the SPN-NCBS5 had absorption and emission in the NIR region (**Supplementary Figs 7** and **9**), the fluorescence was acquired at 780 nm upon excitation at 710 nm (**Supplementary Fig. 7**b shows the spectrum); the afterglow was induced by pre-irradiation at 808 nm.

Next, increasingly thick pieces of chicken tissue were placed on top of the samples, and the signals for both afterglow and fluorescence decreased (**Fig. 4**a,b). However, due to the low background noise for afterglow (824 ± 109 p/s/cm^2/sr) *vs* fluorescence ($2.53 \times 10^7 \pm 1.76 \times 10^6$ p/s/cm^2/sr), the SBR for afterglow (291 ± 18) was 67-times higher than that for fluorescence (4.33 ± 0.96) at a thickness of 1.5 cm. Moreover, the NIR fluorescence was close to the background noise at the thickness of 4 cm, while the SBR for afterglow was still 17.7 ± 0.27. Similarly, the background for afterglow luminescence imaging of a living mouse was as low as 867 ± 80 p/s/cm^2/sr because tissue autofluorescence was eliminated in the absence of real-time excitation. Thus, when detecting the NIR-induced afterglow signals from SPN-NCBS5 at a depth of 1.7 cm through a living mouse (**Fig. 4**c–e), the SBR reached 237 ± 22, which was 4.7- and 120-times higher than the visible-light-induced afterglow (50.7 ± 4.5) and the NIR fluorescence (1.98 ± 0.09), respectively. Importantly, the afterglow could be repeatedly recharged by *in situ* irradiation at 808 nm through chicken tissue or a living mouse

(**Supplementary Figs 15** and **16**) confirming the feasibility of long-term *in vivo* imaging.

The afterglow signals of subcutaneously-implanted SPN-NCBS5 in living mice had a linear correlation with its concentrations (**Supplementary Fig. 17**c). As a result of the high SBR of afterglow, the limit of detection (LOD) of SPN-NCBS5 in living mice was 1.35 ng/mL (**Supplementary Fig. 17**c)—80-times lower than that for NIR fluorescence (**Supplementary Fig. 17**d). Furthermore, the afterglow of SPN-NCBS5 could be preserved at -20 ºC after pre-irradiation, and the intensity only dropped by 3.8% after one day of storage (**Supplementary Fig. 18**). This showed the feasibility of using the pre-irradiated afterglow SPNs directly from storage for *in vivo* imaging with no need for any optical pre-treatment.

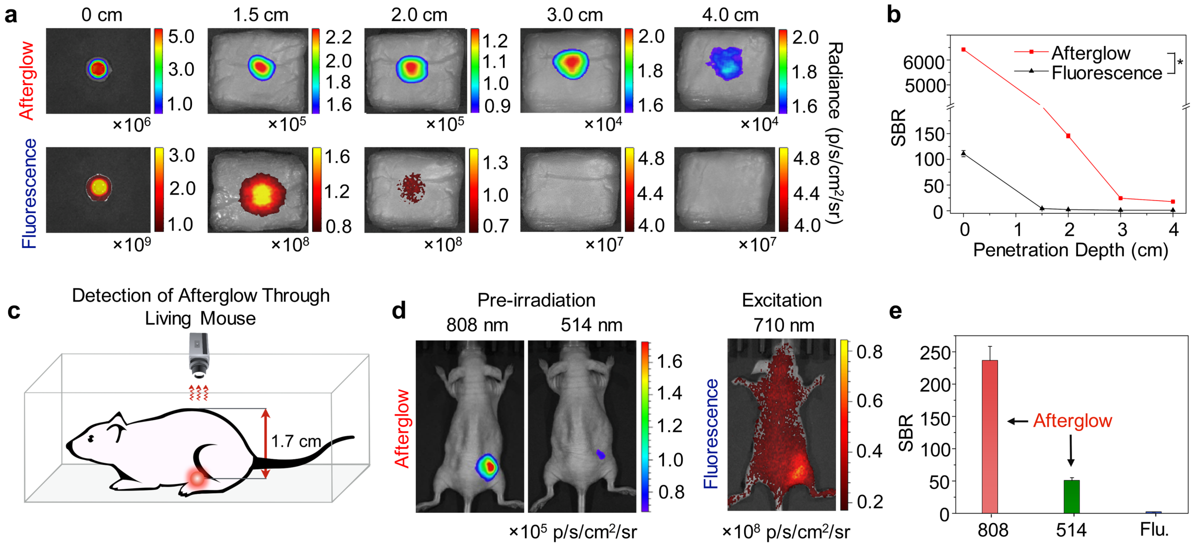

Figure 4. Tissue-penetration study of NIR afterglow luminescence (**a**) Afterglow luminescence (upper panel) and fluorescence (lower panel) imaging of the SPN-NCBS5 solutions through the chicken tissues of different thickness. (**b**) SBRs for afterglow luminescence and fluorescence of SPN-NCBS5 as a function of tissue depth. *Statistically significant difference in SBRs through chicken tissues at 4 cm (n = 3, P < 0.01). **(c)** Schematic illustration of afterglow luminescence imaging through a living mouse, where the SPN-NCBS5 solutions is located under the mouse with a depth of 1.7 cm. (**d**) Afterglow luminescence and fluorescence images of the SPN-NCBS5 solution through a living mouse. The SPN-NCBS5

solutions (62.5 µg/mL, 50 µL) were pre-irradiated with 808 or 514 nm laser (1 W/cm^2) for 1 min and then the images were collected within 5 s after removing the laser. The fluorescence images were acquired at 780 nm upon excitation at 710 nm. (**e**) SBRs for afterglow luminescence and fluorescence imaging in Fig. 4d.

Afterglow Imaging of Lymph Nodes and Tumors

The storable and NIR-renewable afterglow of the amplified SPN (SPN-NCBS5) was used for real-time mapping of lymph nodes in living mice (**Fig. 5a**). Lymph node mapping is clinically important in guiding surgical resection of tumor tissues[30], but has not been achieved with afterglow imaging previously. The pre-irradiated SPN-NCBS5 was stored at -20 ºC for one day, warmed to room temperature, and then directly injected into the forepaw of living mice for continuous imaging without re-irradiation. At t = 30 min post-injection, afterglow and fluorescence images were acquired with an IVIS Spectrum imaging system. The axillary lymph node was clearly delineated with both afterglow and fluorescence imaging (**Supplementary Fig. 19**) indicating an efficient accumulation and retention of SPN-NCBS5 in sentinel lymph nodes. Despite the decay of afterglow over 30 min at 37 ºC in living mice (**Supplementary Fig. 20**a), the SBR of afterglow images was still 7.8 ± 1.2, which is twice as high as the fluorescence images (3.9 ± 0.3) (**Fig. 5**c). After the *in situ* renewal of afterglow at t = 65 min post-injection by irradiation at 808 nm for 1 min, the SBR of afterglow image substantially increased to 419 ± 32: 127-fold higher than fluorescence (**Fig. 5**b,c). Thus, the NIR afterglow of SPN-NCBS5 could map the lymph nodes with high contrast and no need for real-time excitation during imaging.

The afterglow luminescence of SPN-NCBS5 was also tested and compared with NIR fluorescence for passively targeted imaging of tumor in living mice. After tail vein injection of SPN-NCBS5, afterglow and NIR fluorescence signals were acquired in real-time. Both signals gradually increased over time, but the SBR of afterglow images were higher than NIR fluorescence at all time points (**Fig. 5**d, e, f). Due to the low background of afterglow, the tumor was visible at t = 1 h post-injection and clearly visualized at t = 2 h post-injection for afterglow imaging (**Fig. 5**e); in contrast, the tumor could only be visualized at t = 8 h post-injection for NIR fluorescence imaging. At t = 2 h, the SBR of afterglow images was 149.7 ± 9.0—23.3-fold higher than the NIR fluorescence images (6.4 ± 0.9) (**Fig. 5**f). Both afterglow and fluorescence signals plateaued at t = 36 h post-injection indicating the efficient accumulation of SPN-NCBS5 in tumor. The *ex vivo* data further illustrated that SPN-NCBS5 had the highest uptake in liver followed by tumor, lung, and other major organs (**Supplementary Fig. 21**). Thus, the afterglow of SPN-NCBS5 permitted faster and higher contrast imaging of tumor in living mice versus NIR fluorescence imaging.

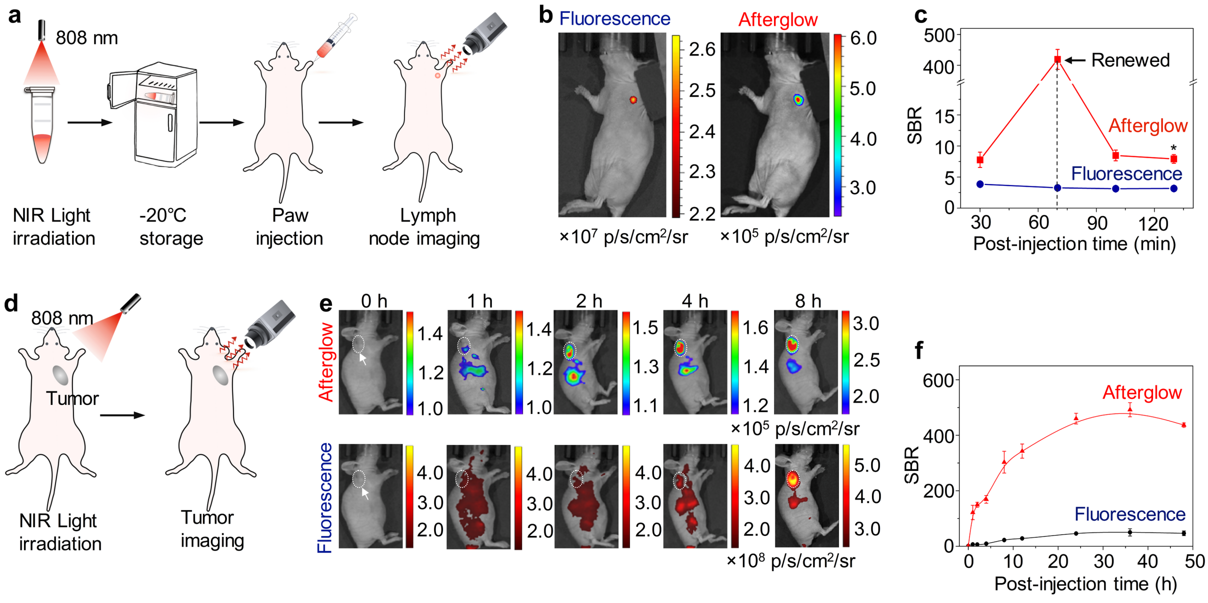

Figure 5. *In vivo* afterglow imaging of lymph nodes and tumor. (**a**) Schematic illustration of afterglow luminescence imaging of lymph node. SPN-NCBS5 was pre-irradiated with an 808 nm laser (1 W/cm^2) for 1 min followed by storage in -20 ºC for one day before being directly used for lymph node imaging. **(b)** Fluorescence (left) and afterglow luminescence (right) imaging of a lymph node in a living mouse at t = 65 min after intradermal injection of

SPN-NCBS5 (0.25 mg/mL, 0.05 mL) into the forepaw of mouse. (**c**) SBRs for afterglow luminescence and fluorescence imaging of lymph node in living mice as a function of post-injection time. *In situ* renewed afterglow of SPN-NCBS5 was conducted at t = 65 min post-injection by irradiation at 808 nm (1 W/cm^2) for 1 min. (**d**) Schematic illustration of afterglow luminescence imaging of xenograft HeLa tumor in mouse models. (**e**) Afterglow luminescence (upper panel) and fluorescence images (lower panel) of tumor in living mice at representative time-points after systemic administration of SPN-NCBS5 (0.25 mg/mL, 0.2 mL) *via* tail vein injection. The tumor was on the right shoulder as indicated by the white dashed circles and arrows. (**f**) SBRs for afterglow luminescence and NIR fluorescence imaging of tumor in living mice as a function of time. Intensity values are the mean ± s.d. for n = 3 mice. The error bars were based on standard deviations (mice n = 3). Afterglow luminescence images were acquired for 180 s after irradiation at 808 nm (0.5 W/cm^2) for 1 min. The fluorescence images were acquired for 0.1 s at 780 nm upon excitation at 710 nm.

Activatable Afterglow Probes for Imaging of Drug-Induced Hepatotoxicity

Drug-induced hepatotoxicity is a long-standing concern of modern medicine[31]. It is one of the most common reasons that the Food and Drug Administration (FDA) withholds drug approval[32]. Evaluation of potential hepatotoxicity in advance of regulatory approval is challenging because current safety assays only accommodate *in vitro* studies and have low predictive power[33]. Oxidative stress and the consumption of antioxidants in the liver are concurrent early events in hepatotoxicity[34]. Among all the antioxidants in living organisms, biothiols including cysteine (Cys), homocysteine (Hcy) and glutathione (GSH) constitute a major portion of the total body antioxidants that defend against oxidative stress. Thus, real-time *in situ* imaging of biothiol levels could be a feasible way to evaluate drug-induced hepatotoxicity.

To develop activatable afterglow probes for biothiol imaging, an amphiphilic oligomer conjugated with an electron-withdrawing quencher (2,4-dinitrophenylsulfonyl, DNBS) was synthesized and coprecipitated with NCBS and MEHPPV (**Fig. 6**a). The resulting activatable nanoprobe (SPN-thiol) had a similar size and morphology as other SPNs (**Supplementary Fig. 22**). Due to the efficient electron transfer from the core to the quencher, the afterglow of the SPN-thiol was substantially quenched at its initial "afterglow off" state (**Fig. 6**a). However, in the presence of biothiols including GSH, Cys and Hcy, the sulfonamide bond on the surface of SPN-thiol could be cleaved, releasing DNBS from the nanoparticle surface. Thus, the electron transfer was abolished leading to activated afterglow ("afterglow on" state). Upon activation by Cys, the afterglow of SPN-thiol at 780 nm increased by 8.3-fold (**Fig. 6**b). This was 1.75- and 1.41-fold higher than GSH and Hcy, respectively. In contrast, the signals remained nearly undetectable for other amino acids (**Fig. 6**c,d). Thus, SPN-thiol had high selectivity towards biothiols particularly Cys. Similar activation was observed for the fluorescence of SPN-thiol (**Supplementary Fig. 23**). In addition, a linear correlation between the afterglow intensities and the concentrations of Cys was observed with a limit of detection (LOD) of 0.60 μM (**Fig. 6**e), which is more than appropriate for *in vivo* biological concentrations of biothiols (~0.1 and 10 mM).

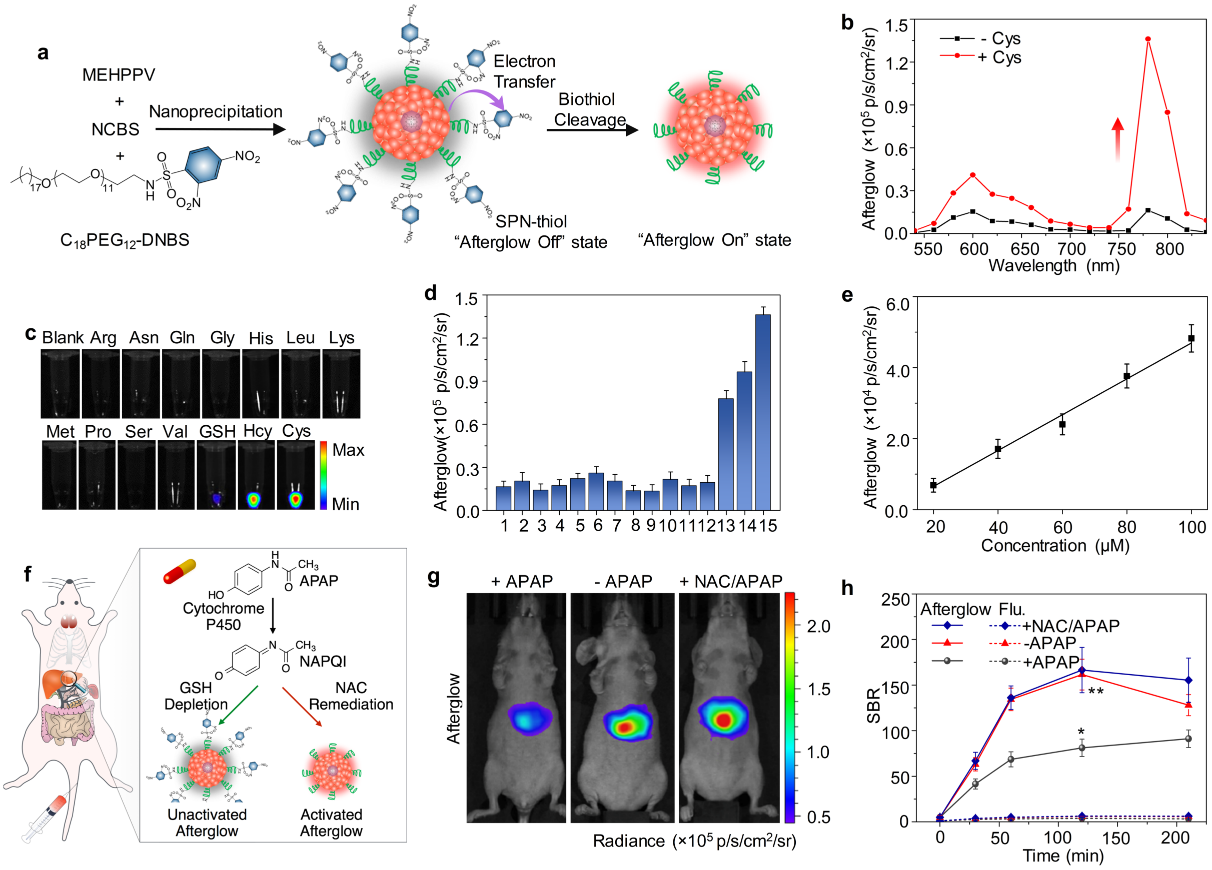

Figure 6. *In vivo* afterglow luminescence imaging of drug-induced hepatotoxicity. (a) Schematic illustration of the design and turn-on mechanism of biothiol-activatable afterglow probe (SPN-thiol). **(b)** Afterglow luminescence spectra of SPN-thiol (12.5 µg/mL) in the absence or presence of Cys (1 mM) in 1×PBS buffer (pH = 7.4). **(c)** Afterglow luminescence images of SPN-thiol (12.5 µg/mL) in the presence of Cys, Hcy, GSH and other amino acids (1 mM) in 1×PBS (pH = 7.4) at 37 ºC. **(d)** Afterglow luminescence intensities of SPN-thiol in the presence of Cys, Hcy, GSH and other amino acids (1 mM) in 1×PBS (pH = 7.4) at 37 ºC. 1: Blank, 2: Arg, 3: Asn, 4: Gln, 5: Gly, 6: His, 7: Leu, 8: Lys, 9: Met, 10: Pro, 11: Ser, 12: Val, 13: GSH, 14: Hcy, 15: Cys **(e)** Fitted calibration curve of the intensity of afterglow luminescence of SPN-thiol as a function of the concentration of Cys. **(f)** Schematic representation of the mechanism of APAP- induced toxicity with the effects of depletion of GSH resulting in the inactivated afterglow and NAC to remediate the depletion to activate the afterglow. **(g)** Representative afterglow luminescence images of mice treated intraperitoneally with APAP (300 mg/kg), saline, or NAC (200 mg/kg) with APAP (300 mg/kg), followed by an intravenous injection of SPN-thiol (0.25 mg/mL, 0.2 mL) at t = 20 min later. Afterglow luminescence images were acquired for 180 s after *in situ* renew by irradiation at 808 nm (1 W/cm^2) for 1 min. **(h)**

SBRs for afterglow luminescence and NIR fluorescence imaging of liver in living mice as a function of time. Intensities values are the mean ± s.d. for n = 3 mice. *Statistically significant difference in the afterglow luminescence intensities between saline- and APAP-treated groups at t = 2 h post-injection of SPN-thiol (n = 3, $P < 0.01$); **No statistically significant differences were seen between saline and APAP/NAC treated groups at t = 2 h post-injection of SPN-thiol (n = 3, $P > 0.05$).

SPN-thiol was used for *in vivo* imaging of drug-induced hepatotoxicity (**Fig. 6**f). Acetaminophen (APAP) is an antipyretic analgesic drug and was utilized as a model drug because the mechanism of APAP-induced hepatotoxicity is well established. An overdose of APAP can induce oxidative and nitrosative stress and in turn deplete biothiols to initiate a signaling cascade resulting in necrotic cell death. The mice were first treated with APAP at the toxic dosage level or saline, and then SPN-thiol was systematically administered *via* intravenous injection at t = 20 min post-treatment of APAP. Afterglow and fluorescence signals were acquired in real-time, and they gradually increased over time (**Fig. 6**h). At t = 2 h post-injection of SPN-thiol, the afterglow of APAP-treated mice was 1.99-times lower than saline-treated control mice (**Fig. 6**g) due to the decreased level of biothiols in liver. In contrast, when the mice were protected with *N*-acetyl-*L*-cysteine (NAC, an FDA-approached antioxidant drug) before APAP treatment, the afterglow signal was comparable to that for the saline-treated control mice. This was attributed to the effective ROS-scavenging ability of NAC to maintain the level of antioxidants in liver. Histological studies further showed massive hepatic necrosis of the livers after 3 h of APAP treatment—no liver lesions were found in the saline-treated control mice or NAC-protected mice (**Supplementary Fig. 26**). The intensity attenuation of afterglow upon APAP treatment and its increase upon NAC remediation confirmed the utility of SPN-thiol for longitudinal imaging of hepatotoxicity *in vivo*. In addition, the SBR ratios of afterglow were ~25-fold higher at all time intervals versus NIR fluorescence (**Fig. 6**h) showing the higher sensitivity of afterglow imaging for drug-induced hepatotoxicity.

Discussion

Light-emitting SPs have been made into nanoparticles and screened for afterglow luminescence imaging applications (**Fig. 1**). The irradiation of certain PPV-based SPNs forms unstable chemical defects (dioxetane units) that can spontaneously and slowly break down to release photons that result in afterglow luminescence (**Fig. 2**g). The formation of dioxetane units within PPVs is the key step towards afterglow. Its efficiency is intrinsically determined by the substituent groups on the vinyl bonds of PPVs. Although the mechanism that governs the afterglow luminescence of PPV-based SPNs resembles chemiluminescence[35], it does not require exogenous ROS to trigger the reaction. Rather, the SPNs themselves can generate $^1O_2$ under light irradiation and subsequently induce afterglow luminescence. Such an afterglow mechanism also differs from that of rare-earth-doped inorganic nanoparticles wherein the absorbed photon energy is stored in intrinsic defect lattices rather than light-induced chemical defects[8].

In addition to temperature control, the afterglow brightness of PPV-based SPNs can be down- or up-regulated by scavenging or promoting the generation of $^1O_2$ (**Fig. 2**f). This principle can fine-tune the afterglow of SPNs by simply doping with NIR-absorbing $^1O_2$ sensitizer so as to amplify afterglow and red-shift both the pre-irradiation and emission wavelengths into the NIR region (**Fig. 3**a). The optimized SPN (SPN-NCBS5) can be pre-irradiated at 808 nm for afterglow emission at 780 nm with absolute brightness that is 74-fold higher than a non-doped SPN (SPN-MEHPPV) (**Fig. 3**f). The NIR absorption of

SPN-NCBS5 also makes it feasible to recharge the afterglow in deep tissue for longitudinal *in vivo* imaging.

As a result of the low background noise in the absence of concurrent light excitation, the NIR afterglow of SPN-NCBS5 has high *in vivo* sensitivity permitting lymph node imaging at a SBR value (419) that is 127-times higher than NIR fluorescence imaging (**Fig 5**b). Moreover, the ultrasensitive NIR afterglow of SPN-NCBS5 allows for faster delineation of tumor within 2 h—this is not possible with NIR fluorescence imaging (**Fig. 5**e). These imaging data clearly prove that afterglow SPNs are promising for image-guided surgical resection of sentinel lymph nodes and tumor tissues. With no need for real-time light excitation, SPN-based afterglow imaging can simplify the instrumentation and potentially offer markedly improved freedom for surgeons.

We report SPN-NCBS5 as water-soluble afterglow nanoparticles. To the best of our knowledge, these materials have the longest emission (780 nm) and half-life (396 s) of all other existing materials; existing rare-earth-doped inorganic nanoparticles have afterglow emission maxima ranging from 610 to 716 nm and half-life times of less than 200 s (**Supplementary Table 1**)[7-16, 36]. Moreover, the *in vivo* NIR afterglow intensity of subcutaneously-implanted SPN-NCBS5 is 5.7×10^5 (p/s/cm^2/sr)/(μg/mL), which is more than two orders of magnitude higher than other types of afterglow nanoparticles, e.g., 5.0×10^3 (p/s/cm^2/sr)/(μg/mL) for subcutaneously-implanted $ZnGa_2O_4$:Cr^{3+} nanoparticles (**Supplementary Table 1**)[10]. With such a strong NIR afterglow, the SBR for the subcutaneously-implanted SPN-NCBS5 in living mice can reach 3387 ± 39 at a concentration of 12.5 μg/mL. This is substantially higher than existing afterglow nanoparticles even when tested at higher concentrations, e.g., $ZnGa_2O_4$:Cr^{3+}

nanoparticles with *in vivo* SBR of 275 at 2 mg/mL (**Supplementary Table 1**)[10] as well as for the Cerenkov luminescence imaging (SBR = 155)[4]. Because of this high SBR, afterglow SPNs permitted *in vivo* imaging of tumors after systemic administration at a much lower dosage (50 µg per mouse) than other existing afterglow agents (200 to 1000 µg per mouse), while still offering a higher SBR.

The structural versatility of SPNs also facilitates the development of a smart activatable afterglow probe (SPN-thiol) for drug-induced hepatotoxicity in living mice (**Fig. 6**). To the best of our knowledge, this is the first demonstration of an afterglow system that changes signal intensity in response to a molecule of interest *in vivo*; existing afterglow nanoparticles have only been used for passive or active tumor targeting (**Supplementary Table 1**). The NIR afterglow of biothiol-activatable probe (SPN-thiol) at 780 nm can be substantially activated via biothiols including Cys, Hcy and GSH (**Fig. 6**d). Because these biothiols are essential antioxidants against oxidative stress, SPN-thiol can detect antioxidant levels in the liver of living mice (**Fig. 6**f) enabling real-time afterglow luminescence imaging of drug-induced hepatotoxicity and remediation at a SBR level that is 25-fold higher than NIR fluorescence imaging. More importantly, SPN-thiol can detect the hepatotoxicity within 20 min of drug challenge, which is much shorter relative to the time required for the observation of histological changes in liver (~3 h)[37]. This proves the capability of SPN-thiol for early-detection of drug-induced hepatotoxicity. With its ideal biodistribution, the afterglow probe could also permit real-time interrogation of the key role of biothiols in other diseases such as cancer and neuroinflammation.

In summary, we have introduced SPNs as a new class of organic afterglow agents for optical imaging in living mice. Due to their unique afterglow mechanism, SPNs can be developed not only as a simple accumulation agent for tissue imaging but also as a smart activatable probe to report the progression of pathological processes in real time in living animals with no need for concurrent light excitation. Due to their organic nature, irradiation and emission both within the NIR window, and facile surface modification, afterglow SPNs have great promise as an advanced molecular imaging tool with sensitivity levels not currently achievable by NIR fluorescence.

Acknowledgements

K.P. thanks Nanyang Technological University (Start-Up grant: NTUSUG: M4081627.120) and Singapore Ministry of Education (Academic Research Fund Tier 1: RG133/15 M4011559 and Academic Research Fund Tier 2 MOE2016-T2-1-098) for the financial support. J.J. thanks NIH HL 137187 and NIH HL 117048 grants for the finical support.

Author contributions

K.P. conceived and designed the study. Q.M. performed the nanoparticle synthesis and *in vitro* experiments. C.X., X.Z. and Q.M. performed the *in vivo* experiments. K.P. and Q.M. contributed to the analysis and interpretation of results and preparation of the manuscript draft. K.P., Q.M., X.L., J.J. and all other authors contributed to the writing of this paper.

Additional information

Supplementary information is available in the online version of the paper. Reprints and permissions information is available online at www.nature.com/reprints. Correspondence and requests for materials should be addressed to K.P.

Competing financial interests

The authors declare no competing financial interests.

References

1. Ntziachristos, V., Ripoll, J., Wang, L.H.V. & Weissleder, R. Looking and listening to light:

the evolution of whole-body photonic imaging. *Nat. Biotechnol.* **23**, 313-320 (2005).

2. Smith, A.M., Mancini, M.C. & Nie, S. Bioimaging: second window for in vivo imaging. *Nat. Nanotechnol.* **4**, 710-711 (2009).
3. Chu, J. *et al*. A bright cyan-excitable orange fluorescent protein facilitates dual-emission microscopy and enhances bioluminescence imaging in vivo. *Nat. Biotechnol.* **34**, 760-767 (2016).
4. Thorek, D.L., Ogirala, A., Beattie, B.J. & Grimm, J. Quantitative imaging of disease signatures through radioactive decay signal conversion. *Nat. Med.* **19**, 1345-1350 (2013).
5. So, M.K., Xu, C., Loening, A.M., Gambhir, S.S. & Rao, J. Self-illuminating quantum dot conjugates for in vivo imaging. *Nat. Biotechnol.* **24**, 339-343 (2006).
6. Liu, H. *et al*. Intraoperative imaging of tumors using Cerenkov luminescence endoscopy: a feasibility experimental study. *J. Nucl. Med.* **53**, 1579-1584 (2012).
7. de Chermont, Q.L. *et al*. Nanoprobes with near-infrared persistent luminescence for in vivo imaging. *Proc. Natl. Acad. Sci. USA* **104**, 9266-9271 (2007).
8. Maldiney, T. *et al*. Controlling electron trap depth to enhance optical properties of persistent luminescence nanoparticles for In vivo imaging. *J. Am. Chem. Soc.* **133**, 11810-11815 (2011).
9. Maldiney, T. *et al*. The in vivo activation of persistent nanophosphors for optical imaging of vascularization, tumors and grafted cells. *Nat. Mater.* **13**, 418-426 (2014).
10. Li, Z.J. *et al*. Direct Aqueous-Phase Synthesis of Sub-10 nm "Luminous Pearls" with Enhanced in Vivo Renewable Near-Infrared Persistent Luminescence. *J. Am. Chem. Soc.* **137**, 5304-5307 (2015).
11. Maldiney, T. *et al*. In vivo optical imaging with rare earth doped $Ca_2Si_5N_8$ persistent luminescence nanoparticles. *Opt. Mater. Express* **2**, 261-268 (2012).
12. Abdukayum, A., Chen, J.T., Zhao, Q. & Yan, X.P. Functional Near Infrared-Emitting Cr^{3+}/Pr^{3+} Co-Doped Zinc Gallogermanate Persistent Luminescent Nanoparticles with Superlong Afterglow for in Vivo Targeted Bioimaging. *J. Am. Chem. Soc.* **135**, 14125-14133 (2013).
13. Liu, F. *et al*. Photostimulated near-infrared persistent luminescence as a new optical read-out from Cr^{3+}-doped $LiGa_5O_8$. *Sci. Rep.* **3**, 1554 (2013).
14. Maldiney, T. *et al*. In vivo imaging with persistent luminescence silicate-based nanoparticles. *Opt. Mater.* **35**, 1852-1858 (2013).
15. Sharma, S.K. *et al*. Persistent luminescence of $AB_2O_4:Cr^{3+}$ (A = Zn, Mg, B = Ga, Al) spinels: New biomarkers for in vivo imaging. *Opt. Mater.* **36**, 1901-1906 (2014).
16. Shi, J.P. *et al*. Multifunctional near infrared-emitting long-persistence luminescent nanoprobes for drug delivery and targeted tumor imaging. *Biomaterials* **37**, 260-270 (2015).
17. Toppari, J. *et al*. Male reproductive health and environmental xenoestrogens. *Environ. Health Perspect.* **104 Suppl 4**, 741-803 (1996).
18. Kobayashi, H. & Choyke, P.L. Target-cancer-cell-specific activatable fluorescence imaging probes: rational design and in vivo applications. *Acc. Chem. Res.* **44**, 83-90 (2011).
19. Lovell, J.F., Liu, T.W., Chen, J. & Zheng, G. Activatable photosensitizers for imaging and therapy. *Chem. Rev.* **110**, 2839-2857 (2010).
20. Feng, L. *et al*. Conjugated polymer nanoparticles: preparation, properties, functionalization

and biological applications. *Chem. Soc. Rev.* **42**, 6620-6633 (2013).

21. Wu, C. & Chiu, D.T. Highly fluorescent semiconducting polymer dots for biology and medicine. *Angew. Chem. Int. Ed.* **52**, 3086-3109 (2013).
22. Qian, C. *et al.* Light-Activated Hypoxia-Responsive Nanocarriers for Enhanced Anticancer Therapy. *Adv. Mater.* **28**, 3313-3320 (2016).
23. Zhen, X. *et al.* Intraparticle Energy Level Alignment of Semiconducting Polymer Nanoparticles to Amplify Chemiluminescence for Ultrasensitive In Vivo Imaging of Reactive Oxygen Species. *ACS Nano* **10**, 6400-6409 (2016).
24. Pu, K.Y. *et al.* Semiconducting polymer nanoparticles as photoacoustic molecular imaging probes in living mice. *Nat. Nanotechnol.* **9**, 233-239 (2014).
25. Hong, G. *et al.* Ultrafast fluorescence imaging in vivo with conjugated polymer fluorophores in the second near-infrared window. *Nat. Commun.* **5**, 4206 (2014).
26. Lyu, Y., Xie, C., Chechetka, S.A., Miyako, E. & Pu, K. Semiconducting Polymer Nanobioconjugates for Targeted Photothermal Activation of Neurons. *J. Am. Chem. Soc.* **138**, 9049-9052 (2016).
27. Ghezzi, D. *et al.* A hybrid bioorganic interface for neuronal photoactivation. *Nat. Commun.* **2**, 166 (2011).
28. Palner, M., Pu, K., Shao, S. & Rao, J. Semiconducting Polymer Nanoparticles with Persistent Near-Infrared Luminescence for In Vivo Optical Imaging. *Angew. Chem. Int. Ed.* **54**, 11477-11480 (2015).
29. Scurlock, R.D., Wang, B.J., Ogilby, P.R., Sheats, J.R. & Clough, R.L. Singlet Oxygen as a Reactive Intermediate in the Photodegradation of an Electroluminescent Polymer. *J. Am. Chem. Soc.* **117**, 10194-10202 (1995).
30. Kim, S. *et al.* Near-infrared fluorescent type II quantum dots for sentinel lymph node mapping. *Nat. Biotechnol.* **22**, 93-97 (2004).
31. Nasr, A., Lauterio, T.J. & Davis, M.W. Unapproved drugs in the United States and the Food and Drug Administration. *Adv. Ther.* **28**, 842-856 (2011).
32. Kola, I. & Landis, J. Can the pharmaceutical industry reduce attrition rates? *Nat. Rev. Drug Discov.* **3**, 711-715 (2004).
33. Willmann, J.K., van Bruggen, N., Dinkelborg, L.M. & Gambhir, S.S. Molecular imaging in drug development. *Nat. Rev. Drug Discov.* **7**, 591-607 (2008).
34. Pessayre, D., Mansouri, A., Berson, A. & Fromenty, B. Mitochondrial involvement in drug-induced liver injury. *Handb. Exp. Pharmacol.*, 311-365 (2010).
35. Dodeigne, C., Thunus, L. & Lejeune, R. Chemiluminescence as a diagnostic tool. A review. *Talanta* **51**, 415-439 (2000).
36. Maldiney, T. *et al.* Effect of Core Diameter, Surface Coating, and PEG Chain Length on the Biodistribution of Persistent Luminescence Nanoparticles in Mice. *ACS Nano* **5**, 854-862 (2011).
37. Shuhendler, A.J., Pu, K.Y., Cui, L., Uetrecht, J.P. & Rao, J.H. Real-time imaging of oxidative and nitrosative stress in the liver of live animals for drug-toxicity testing. *Nat. Biotechnol.* **32**, 373-380 (2014).